Equilibrium structure and lateral stress distribution of amphiphilic bilayers from dissipative particle dynamics simulations

Julian C. Shillcock[a)] and Reinhard Lipowsky

Max-Planck-Institut für Kolloid- und Grenzflächenforschung, 14424 Potsdam, Germany

The equilibrium structure and lateral stress profile of fluid bilayer membrane patches are investigated using the Dissipative Particle Dynamics simulation technique. Although there are no attractive forces between the model amphiphiles, they spontaneously aggregate into planar bilayers under suitable conditions of concentration and amphiphile architecture. Pure bilayers of single-chain and double-chain amphiphiles are simulated, and the amphiphile architecture and interaction parameters varied. We find that a strong chain stiffness potential is essential to create the lamellar order typical in natural lipid membranes. Single-chain amphiphiles form bilayers whose lamellar phase is destabilized by reductions in the tail stiffness. Double-chain amphiphiles form bilayers whose rigidity is sensitive to their architecture, and that remain well-ordered for smaller values of their tail stiffness than bilayers of single-chain linear amphiphiles with the same hydrophobic tail length. The lateral stress profile across the bilayers contains a detailed structure reflecting contributions from all the interaction potentials, as well as the amphiphile architecture. We measure the surface tension of the bilayers, and extract estimates of the membrane area stretch modulus and bending rigidity that are comparable to experimental values for typical lipid bilayers. The stress profile is similar to that found in coarse-grained Molecular Dynamics simulations, but requires a fraction of the computational cost. Dissipative Particle Dynamics therefore allows the study of the equilibrium behavior of fluid amphiphilic membranes hundreds of times larger than can be achieved using Molecular Dynamics simulations, and opens the way to the investigation of complex mesoscopic cellular phenomena. © *2002 American Institute of Physics.*
[DOI: 10.1063/1.1498463]

I. INTRODUCTION

Lipid bilayer membranes surround living cells, protecting their interior from the outside world. They are much more than a static structural component, however, in that their composition and dynamics influence membrane-bound proteins, and contribute to the remarkable material properties of cells such as red blood cells.[1,2] Bilayer membranes also surround artificial vesicles, and have been constructed out of nonbiological amphiphiles,[3,4] and diblock copolymers.[5] These membranes continually undulate owing to the thermal motion of their constituent lipids. Thermal forces combine with specific molecular forces to create complex, dynamic, multicomponent systems. Dynamic processes taking place within a membrane can involve cooperative changes over distances large compared to the molecular size, and occur on timescales much longer than molecular vibrational periods.

The complexity of natural membranes has led experimentalists to focus on simpler model systems: lipid bilayer vesicles.[6–10] These are often composed of a single type of amphiphile, and usually lack embedded inclusions. Much progress has been made in the last decade in experiments designed to probe the vesicle membrane's material properties. The area stretch modulus of pure stearoyloleoylphosphatidylcholine (SOPC) vesicles and SOPC/cholesterol mixtures has been measured using micropipette aspiration,[11] and

is found to increase on adding cholesterol as a cosurfactant. The lateral diffusion of lipids in a vesicle membrane[12] and the membrane viscosity[13] have both been recently determined. Detailed studies have been published of the dependence of the bilayer elastic bending and area stretch moduli[14] and passive permeability[15] on lipid tail length and the degree of unsaturation. Dynamic light scattering has been used to measure vesicle shape fluctuations, and the increase in the fluctuation time on the addition of small amounts of cosurfactant.[16] Domain formation in two-component lipid membranes has also been investigated.[17] Nonbiological amphiphiles have been used to provide a template for the construction of nanoscale, hollow, polymeric spheres.[18] Amphiphilic diblock copolymers have been shown to form vesicles that are an order of magnitude stronger, and less permeable to water, than natural phospholipid bilayers.[5] Such toughened vesicles, or polymersomes, offer greater control over the membrane material properties than lipid vesicles, owing to the possibility of cross-linking the copolymers and changing the block size or molecular weight. Lyotropic mesophases of similar diblock copolymers have been used as templates for forming mesoporous silica materials, with the result that the lyotropic order is retained in the silica matrix.[19]

Such experiments have created a demand for a theoretical understanding of the dependence of membrane stability and material properties on the constituent amphiphile's mo-

a)Electronic mail: julian@mpikg-golm.mpg.de

      5048

lecular structure and membrane composition. Several theoretical approaches have been applied to this problem. Lattice-based Monte Carlo (MC) simulations have been used to study the development of microstructures in surfactant–water systems,[20] and the conformational chain properties of lipids within a bilayer composed of long or short chain molecules, and a mixture of both.[21] Several groups have applied mean-field techniques to lipid bilayers,[22–24] exploring the dependence of membrane stability on key lipid properties such as the area per head group[25] and hydrocarbon tail length[21] and the variation of membrane bending stiffness with amphiphile tail length and head group area.[26] Charged lipids and their interactions with ions near the solvent–membrane interface have also been investigated using a self-consistent field theory.[27]

Both these approaches have certain limitations. Lattice-based simulations lack the full Galilean invariance of a fluid, while mean-field theories ignore fluctuations within a system. Furthermore, atomistic Molecular Dynamics (MD) simulations are restricted to small system sizes and short times.[28] Therefore, coarse-grained MD simulations have been used to extract the area compression modulus and bending modulus of single-component lipid bilayers and monolayers, and their lateral stress distribution.[29–32] The latter quantity is believed to be important in modulating membrane–bound protein behavior.[33] Recently, coarse-grained MD simulations have also been used to compare the equilibrium structure of a dimyristoylphosphatidycholine bilayer[34] to that obtained from atomistic simulations. This provides the opportunity to move up in length scale toward the mesoscopic regime. However, a major drawback of even these MD simulations is that they are restricted by current computing technology to membrane patches containing only a few hundred amphiphiles plus the requisite solvent molecules.

In this paper, we use the Dissipative Particle Dynamics (DPD) simulation method to investigate the structure and lateral stress profile of fluid bilayer membranes containing approximately 3200 amphiphiles as a function of the amphiphile architecture and interaction parameters. This represents a membrane patch at least one order of magnitude larger than previously published results,[35,36] and allows us to study the membrane's mesoscopic properties while the (presumably) irrelevant short length-scale motions of the individual amphiphiles are averaged out. Although the DPD technique was first introduced almost a decade ago,[37] and several theoretical analyses of the methodology have appeared,[38–41] published applications are still few. It has been used to measure the surface tension of a planar interface between two polymeric fluids;[42] to study microphase separation of diblock copolymer melts;[43] and to follow the detachment of an oil droplet from a solid surface under shear flow.[44] Self-assembly of a small bilayer patch, containing only 100 surfactants, has also been described.[35] A very recent paper[36] investigates the appearance of pores in model lipid bilayers as a function of the concentration of a nonionic cosurfactant. A recent review article provides a comprehensive survey of computer simulations of surfactant solutions,[45] and another is devoted to the DPD method.[46] Our aim in this

work is to determine whether DPD simulations can take the investigation of membrane material properties to length and time scales beyond those achievable in coarse-grained MD simulations, while still exhibiting the structure found in lateral stress profiles. We have varied the amphiphile architecture and the potential parameters so as to systematically examine their effects on the equilibrium bilayer structure, and to extend the scope of DPD simulations well beyond previous work[35,36] in the field. Given that a micron-size vesicle can contain from one million to a billion amphiphiles, and that a few percent of its surface area is involved in processes such as pore formation or fusion events, the ability to model large systems is essential if these processes are to be studied using computer simulations. Nanoscale vesicle templating[18,19] also requires the simulation of large membrane patches or, preferably, a complete vesicle, that are currently beyond the reach of the coarse-grained MD technique.

The paper is organized as follows. We first briefly review the Dissipative Particle Dynamics simulation technique, referring the interested reader to Ref. 42 for a detailed description. Then we present the equilibrium bilayer structure and stress profile of single-tail amphiphile bilayers as a function of the tail length and interaction parameters. Next, we extend these results to bilayers composed of double-tailed amphiphiles, and study the effects of architecture on the stress profile. Finally, we discuss the implications of this work for simulating complex processes in lipid bilayers.

II. DISSIPATIVE PARTICLE DYNAMICS SIMULATION METHOD

The elementary units in a DPD simulation are fluid elements or *soft beads*. A soft bead represents a volume of fluid that is large on a molecular scale, and hence contains at least several molecules or molecular groups, but still macroscopically small. Beads interact via effective forces chosen so as to reproduce the hydrodynamic behavior of the fluid without reference to its molecular structure. DPD differs in this respect from MD simulations, in which the forces are chosen to model the intermolecular interactions of a system as accurately as possible. Forces in DPD are pairwise additive, conserve momentum, have no hard core, and are short-ranged, the range of the force defining the size of the soft beads. The use of momentum-conserving forces also distinguishes DPD from Brownian Dynamics, in which each particle receives a random push independently of all other particles resulting in purely diffusive motion.

All beads have the same mass, m_0, and radius, r_0, and these set the mass and length scales in the simulation. A time scale must be extracted from the dynamics of relevant processes in the simulated fluid, such as the diffusion of a micelle's center of mass, or the in-plane viscosity of a bilayer membrane. Because we study equilibrium properties of bilayers, we estimate the time scale of the simulations from the generic time, $t_0 = \sqrt{m_0 r_0^2 / k_B T}$, set by the bead mass and radius and the system temperature, where k_B is Boltzmann's constant and the temperature T is defined in the next section. We take the diameter of one DPD bead as 1 nm and assume that it has the density of water at room temperature, T

$=300$ K. The simulation time step then corresponds to 5 ps, and a typical run of 10^5 steps is equivalent to 25 ns of real time. A few longer runs of 0.25 μs have also been performed with equivalent results.

A. Interaction potentials and amphiphile architecture

Beads interact via three forces: a conservative force that gives each bead an identity and allows, for example, the representation of hydrophobicity between hydrocarbon and water; a random force that creates relative momentum between bead pairs; and a dissipative force that destroys relative momentum. Beads are considered to have (unobserved) internal degrees of freedom that give rise to the dissipative force, and to be coupled to the local temperature of their (fluid) environment that is the source of the random forces. By deriving the Fokker–Planck equation equivalent to the Langevin formulation of DPD, and demanding that the steady-state solution satisfy the Gibbs canonical ensemble, Espagnol and Warren[38] have shown that the magnitudes of the dissipative and random forces must be related to the temperature parameter by a fluctuation–dissipation theorem. This relation, together with the requirement that the compressibility of a one-component DPD fluid match that of water at room temperature, fixes the relative strengths of the random and dissipative forces and the ratio of the conservative force parameter (for a one-component fluid) to the temperature. Groot and Warren[42] further show how the magnitude of the conservative force between unlike DPD beads in a fluid mixture is related to the solubility of one species in the other, and how this can be quantified by comparing the solubility of dissimilar DPD fluids with the Flory–Huggins theory of immiscible polymers. For further information on this point the interested reader is referred to the original references.[38,42]

All forces between DPD beads conserve momentum locally, and the expected hydrodynamic behavior, e.g., the drag force exerted on a fixed cylinder by a moving fluid,[37] emerges, even for systems containing only a few hundred beads. To establish this behavior using MD requires prohibitively large simulations.

The conservative force between two beads i and j separated by a distance r_{ij} is

$$\mathbf{F}_{ij}^C = a_{ij}(1 - r_{ij}/r_0)\hat{\mathbf{r}}_{ij}, \tag{1}$$

for $r_{ij} < r_0$, and zero otherwise. The range of the force is set by r_0 and a_{ij} is the maximum repulsion between beads of types i, j, r_{ij} is the distance between the centers of beads i, j, and $\hat{\mathbf{r}}_{ij}$ the unit vector pointing from bead j to bead i. The conservative force is always finite, taking its maximum value at zero separation, and is repulsive for positive a_{ij}.

The dissipative force between two beads is linear in their relative momentum and takes the form

$$\mathbf{F}_{ij}^D = -\gamma_{ij}(1 - r_{ij}/r_0)^2(\hat{\mathbf{r}}_{ij}\cdot\mathbf{v}_{ij})\hat{\mathbf{r}}_{ij}, \tag{2}$$

for $r_{ij} < r_0$, and zero otherwise, where γ_{ij} is the strength of the dissipation between beads i, j, and $\mathbf{v}_{ij} = \mathbf{v}_i - \mathbf{v}_j$ is their relative velocity (or momentum as $m_0 = 1$ in our simulations).

Finally, the random force between a bead pair is

$$\mathbf{F}_{ij}^R = \sqrt{2\gamma_{ij}k_B T}(1 - r_{ij}/r_0)\zeta_{ij}\hat{\mathbf{r}}_{ij}, \tag{3}$$

for $r_{ij} < r_0$, and zero otherwise. Values of the random force are generated by sampling a uniform random variable, $\zeta_{ij}(t)$, that satisfies $\langle\zeta_{ij}(t)\rangle = 0$ and $\langle\zeta_{ij}(t)\zeta_{i'j'}(t')\rangle = (\delta_{ii'}\delta_{jj'} + \delta_{ij'}\delta_{ji'})\delta(t - t')$. The random force has the symmetry property $\zeta_{ij}(t) = \zeta_{ji}(t)$ that ensures local momentum conservation and hence the correct hydrodynamic behavior of the simulated fluid on long length scales.[32]

Polymers are constructed by tying beads together using Hookean springs with the potential

$$U_2(i, i+1) = (1/2)k_2(|\mathbf{r}_{ii+1}| - l_0)^2, \tag{4}$$

where i, $i+1$ represent adjacent beads in the polymer. The spring constant, k_2, and unstretched length, l_0, are chosen so as to fix the average bond length to a desired value. Both parameters may be specified independently for each bead pair, allowing a polymer's bond strength to vary along its length.

Hydrocarbon chain stiffness is modeled by a three-body potential acting between adjacent bead triples in a chain,

$$U_3(i-1, i, i+1) = k_3[1 - \cos(\phi - \phi_0)], \tag{5}$$

where the angle ϕ is defined by the scalar product of the two bonds connecting beads $i-1$, i, and i, $i+1$. In general, the bending constant, k_3, and preferred angle, ϕ_0, may be specified independently for different bead triples, allowing chain stiffness to vary along the polymer's length. Typically, a preferred angle of zero is used so that the potential minimum occurs for parallel bonds in a chain.

Various polymer architectures are used to represent bilayer-forming amphiphiles. They are composed of hydrophilic head beads, designated H, and hydrophobic tail or chain beads, designated C. The simplest architecture has a single H bead attached to a linear chain of C beads. The number of chain beads is varied to investigate the dependence of bilayer properties on the degree of amphiphile hydrophobicity. An amphiphile containing one head and n chain beads is represented, using an obvious symbolism, as HC_n. Biological lipid molecules often possess two hydrocarbon tails, and have head groups of different degrees of bulkiness. A simple architecture that reflects these properties consists of a number m of hydrophilic head beads attached to two linear hydrophobic tails, each containing n chain beads. Such amphiphiles are designated $H_m(C_n)_2$. Both tails may be connected to a single hydrophilic bead, which is designated the head of the amphiphile, to which the remaining hydrophilic beads are also attached, or the tails may be attached to adjacent head beads. The former arrangement creates a more bulky head group than the latter and forces the hydrophobic tails closer together. The amphiphiles are contained within bulk solvent composed of W beads. Each solvent bead represents a small volume of bulk water consisting of several molecules. Because each W bead represents several molecules of solvent, there is no explicit modeling of hydrogen bonds or entropic forces. The beads in DPD simulations are to be interpreted as a coarse graining of a fluid rather than a simulation of the atoms of a fluid. In this way,

TABLE I. Bead–bead conservative force parameters, a_{ij} (in units of $k_B T/r_0$), dissipative force parameters, γ_{ij} (in units of $\sqrt{m_0 k_B T/r_0^2}$), and Hookean bond potential parameters, k_2, l_0 (in units of $k_B T/r_0^2$, r_0, respectively) for all bead pairs. Water is slightly repelled from the amphiphile head, and its strong repulsion from the amphiphile tail provides the hydrophobic interaction needed to form the bilayer. The amphiphile head is hydrophilic and so repelled somewhat from its tail. The bond strength parameters apply to bonds joining the stated beads, e.g., $k_2 = 128$ for HC and CC bonds. Water is represented as a single bead and has no bond parameters. Note that not all amphiphile architectures require all these parameters. They are grouped together here for completeness.

Bead Pairs	a_{ij}	γ_{ij}	k_2	l_0
HH	25	4.5	128	0.5
CC	25	4.5	128	0.5
WW	25	4.5	0	0
HW	35	4.5	0	0
HC	50	9	128	0.5
CW	75	20	0	0

TABLE II. Alphabetical list of symbols used in the text.

Symbol	Description
A	Bilayer area
A_{pr}	Bilayer projected area
a_{ij}	Conservative force parameter between beads i,j
C	Hydrophobic bead composing amphiphile chain(s)
δ_{ij}	Kronecker delta function
$\delta(t-t')$	Dirac delta function
$\mathbf{F}_{ij}^C$	Conservative force between beads i,j
$\mathbf{F}_{ij}^D$	Dissipative force between beads i,j
$\mathbf{F}_{ij}^R$	Random force between beads i,j
γ_{ij}	Dissipative force parameter between beads i,j
H	Hydrophilic bead composing amphiphile headgroup
k_B	Boltzmann's constant
k_2	Hookean bond strength for adjacent beads in an amphiphile
k_3	Chain stiffness for adjacent bonds in an amphiphile
κ	Bilayer bending modulus
K	Bilayer area stretch modulus
l_0	Hookean bond unstretched length
ℓ_{me}	Membrane thickness measured from head group to head group
ℓ_{ee}	Amphiphile end-to-end length
L_X, L_Y, L_Z	Simulation box side lengths
m	Number of hydrophilic beads in amphiphile head group
m_0	Bead mass
n	Number of hydrophobic beads in one chain of an amphiphile
N	Total number of DPD beads in simulation
ϕ_0	Preferred angle between adjacent bonds in a stiff chain
r_0	Bead radius
r_{ij}	Distance between beads i,j
$\mathbf{r}_{ij}$	Relative position vector joining beads i,j
$\hat{\mathbf{r}}_{ij}$	Unit vector between beads i,j
ρ	Number of beads per unit volume in the simulation box
σ	Bilayer surface tension
T	Temperature parameter
$U_2(i,i+1)$	Bond potential between adjacent beads $i,i+1$ in an amphiphile
$U_3(i-1,i,i+1)$	Bending potential between adjacent bead triples $i-1,i,i+1$ in an amphiphile
$\mathbf{v}_{ij}$	Relative velocity of beads i,j
W	Solvent bead
ζ_{ij}	Random force between beads i,j

only structure and behavior that occur on length scales larger than the soft beads have physical relevance. Further, because the bead–bead interactions are soft, we do not attempt to model the liquid crystal–gel phase transition of lipid hydrocarbon chains, and work well within the fluid region of the model amphiphile phase diagram.

We refer to the polymers as surfactants or amphiphiles rather than lipids both to emphasize the generality of the simulation technique and to avoid suggesting that the model amphiphiles should be viewed as atomically detailed representations of the complex structure of lipid molecules. Groot and Warren[42] have shown how the equivalent Flory–Huggins χ parameter for a mixture of immiscible DPD polymers may be extracted from their segregation and related to the polymer length. Because the DPD beads used here have no internal structure, and thus do not incorporate small length-scale molecular characteristics such as polarizability, we treat the glycerol–phosphate-head region of a lipid as a single hydrophilic head bead for the linear amphiphiles, HT_n, and a linear sequence of head beads for $H_m(C_n)_2$. The lipid hydrocarbon tails are represented as linear chains of hydrophobic beads. The number of tail beads per amphiphilic chain is mapped onto the length of actual lipid molecules by comparing the bilayer width and lipid end-to-end length with their known values from experiments, and is presented in Sec. III B. For concreteness, this mapping results in one DPD chain bead corresponding to three to four methyl groups. The same interpretation applies to nonbiological amphiphiles, such as alkyl phosphate surfactants[3] that consist of a single carbon chain attached to a phosphate head group.

The Hookean bonds and chain stiffness parameters are identified by the names of the beads defining them. Hence, an HC_6 amphiphile requires two bond types, HC and CC, and allows two possible chain stiffness potentials, HCC and CCC. The Hookean spring constant, k_2, cannot be zero in an amphiphile, but the chain stiffness, k_3, may be zero. A nonzero chain stiffness represents the nonideal chain character of hydrocarbon tails. Table I summarizes all the bead–bead force parameters and Hookean bond strengths used. Also see Table II. The chain stiffness potential parameters are speci-

fied as needed in the text. Note that not all the parameter values shown are needed for all amphiphile architectures.

B. Simulation parameters

Simulations take place within a cuboidal box of constant volume $V = L_X L_Y L_Z$, where L_X, L_Y, L_Z are the simulation box side lengths in units of the bead diameter, r_0. Periodic boundary conditions are used in all three dimensions to minimize edge effects. The simulation box is filled with beads to the chosen density, which represents ρ beads/unit volume. We are interested in studying the properties of a single bilayer in water. The number of amphiphiles in the bilayer, N, is determined by the box area, $L_X L_Y$, and the desired projected area per amphiphile, A_{pr}/N according to $N = 2L_X L_Y/(A_{pr}/N)$. Because the bead radius, r_0, defines the length scale for the simulations, we quote dimensional quan-

tities in their dimensionless form, e.g., the true area per amphiphile (measured using an algorithm described in Sec. III A, and equal to A_{pr}/N for a flat bilayer), is $\langle A \rangle / N r_0^2$. In a similar manner, the mass and time scales are obtained from the bead mass and radius, and the system temperature.

Once the amphiphile architecture and interaction potentials have been specified, the Newtonian equations of motion of the beads are integrated, and samples of the bilayer properties are collected for analysis after allowing initial transients to decay. The first 50 000 configurations are typically excluded from analysis to ensure that the influence of the initial state is negligible. Observables are constructed from at least 1000 independent samples of bead coordinates. Because of the soft potentials in DPD, the correlation times for bead properties are very short, typically only a few tens of time steps, and samples are taken every 50 time steps. A typical run of 10^5 steps for a bilayer containing 3200 amphiphiles takes 72 CPU hours on a Compaq Alpha ES400 processor.

Random initial configurations are created by assigning random position coordinates to all beads, subject to the constraint that adjacent beads in an amphiphile are not separated by more than a bead diameter to prevent artificially large forces occurring in the initial state. Bead momenta are then assigned from a Maxwell distribution whose temperature corresponds to that defined by the ratio of the dissipative and random force constants. A bilayer initial configuration is created by specifying the number of amphiphiles in the bilayer and placing the heads of pairs of amphiphiles on the sites of two parallel hexagonal lattices representing the outer surfaces of two apposed monolayers. The amphiphiles are oriented so that their head beads face out into the water and their tails point into the bilayer bulk. In all initial states, sufficient water beads are randomly distributed throughout empty regions of the simulation box to achieve the chosen density ρr_0^3.

III. RESULTS

The simplest amphiphile architecture that is found to self-assemble into a bilayer consists of a single, hydrophilic head bead attached to a linear chain of hydrophobic chain beads designated HC_n. A snapshot of a bilayer composed of HC_6 amphiphiles is shown in Fig. 1. The simulation box size is $V/r_0^3 = 32^3$, and the overall bead density is $\rho r_0^3 = 3$, giving approximately 100 000 beads of all types. A bilayer readily self-assembles when the amphiphiles are initially randomly distributed in water for surfactant number fractions in the fairly restricted range of 3%–6%. Below this range micelles occur, and above it complicated three-dimensional structures are formed (data not shown). Unlike recent coarse-grained MD simulations,[29–32,34] there are no attractive forces between amphiphiles in our DPD simulations. The absence of attractive forces is not essential, but their presence is found to be unnecessary in obtaining well-ordered bilayer membranes whose properties agree at least qualitatively with coarse-grained MD simulations. The amphiphiles aggregate into a bilayer because of the strong repulsion between the chain beads and the solvent beads, mimicking the hydropho-
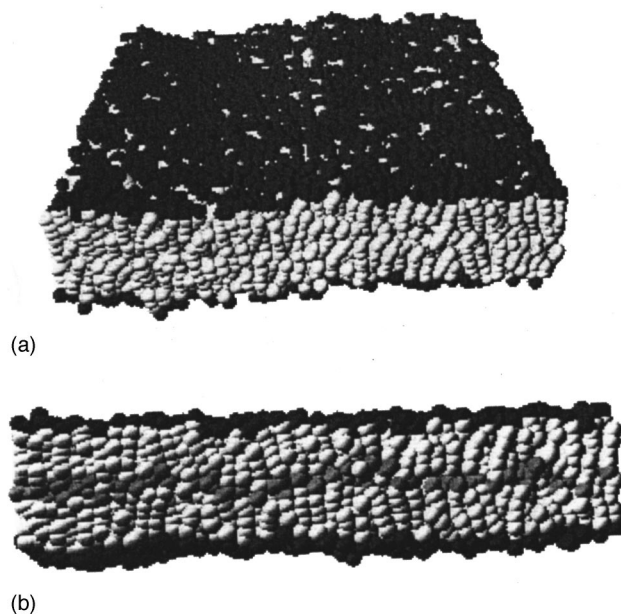

(a)

(b)

FIG. 1. (a) Snapshot of a bilayer containing 3321 HC_6 amphiphiles. The simulation box has size $(32 r_0)^3$, and the bead density is $\rho r_0^3 = 3$, giving almost 100 000 beads of all types. The projected area per amphiphile is $A_{pr}/N r_0^2 = 0.616$, leading to a surface tension of $\sigma = 0.02 \pm 0.04$. This is an average value obtained from repeated simulations of the same bilayer, as described in the text. The amphiphile head beads are dark gray, and the chain beads are light gray. The average membrane thickness, measured from the center of the head beads of one monolayer to those of the other, is $\langle \ell_{me} \rangle / r_0 = 6.61 \pm 0.01$. Water beads are invisible for clarity. (b) Snapshot of another simulation of the system in (a) except that the terminal chain bead is colored darker to demonstrate that the amphiphiles terminate near the bilayer midplane, and form two relatively non-interdigitated monolayers. Thermally excited shape fluctuations are small because of the amphiphile chain stiffness.

bic force of, for example, lipid hydrocarbon tails in water. The absence of attractive forces between amphiphile tails does, however, influence the structure of the bilayer's hydrophobic region, a point we discuss in more detail in the next section. Because of the large parameter space of the simulations, we investigate the effects of just a few parameter combinations. Given three bead types (H, C and W), there are six independent bead–bead conservative interaction parameters. We follow the procedure of Ref. 42 and fix the self-interactions, a_{HH}, a_{CC}, a_{WW}, from the requirement that a pure fluid of each bead type has the compressibility of water. The beads are connected into semiflexible polymers using a bond potential and a chain bending potential that contribute two more parameters each. We fix the spring constant and unstretched bond length to $k_2 r_0^2 / k_B T = 128$ and $l_0 = 0.5 r_0$, respectively, and the preferred bond angle to 0. This choice of values leads to well-ordered bilayers and is explained in the next section. This leaves four parameters to be investigated: a_{HC}, a_{HW}, a_{CW}, and $k_3 / k_B T$ in addition to the number density of amphiphiles. We have not investigated the effects of varying the dissipation coefficients, γ_{ij}, because they are irrelevant for the equilibrium structures we are interested in.[42] Instead, they are chosen to yield a well-ordered bilayer. Because of the periodicity of the simulation box, bilayers do not always assemble with the same orientation, but to simplify the discussion we refer to the bilayer normal as the Z

axis in all our results. A small bilayer containing 830 amphiphiles in an area $(16r_0)^2$ readily self-assembles from an initially random configuration in 20 000 time steps (data not shown). Because the self-assembly of bilayers has been studied previously,[28–32,35] and we are interested in measuring equilibrium properties of large membranes, we preassemble the amphiphiles into a planar bilayer, and allow it to relax to an equilibrium state before constructing ensemble averages of observables.

A. Structural properties of bilayers of linear amphiphiles

The bilayer shown in Fig. 1 contains 3321 HC_6 amphiphiles and has a relaxed area per amphiphile of $\langle A \rangle / N r_0^2 = 0.63 \pm 0.01$, and an approximately zero surface tension, $\sigma r_0^2 / k_B T = 0.02 \pm 0.04$ (see the next section for the measurement of surface tension and error analysis). The snapshots in Figs. 1(a) and 1(b) come from separate simulations with identical parameters, but the terminal chain bead is colored differently from the intermediate chain beads in Fig. 1(b) to show that the amphiphiles terminate near the bilayer midplane. Previous studies of bilayer geometric properties[29–32,35] have used the projected area, $A_{pr}/N r_0^2$, obtained by dividing the simulation box area by one-half of the amphiphiles. This projected area differs from the true or intrinsic area when the bilayer undergoes thermally excited shape fluctuations, or the numbers of amphiphiles in the monolayers are significantly different. For the bilayer shown in Fig. 1, the projected area is $A_{pr}/N r_0^2 = 0.616$, quite close to the relaxed area, as the bilayer is almost flat. To ensure greater accuracy for undulating bilayers, we measure the bilayer thickness and area from a triangulation of the two monolayer surfaces. A rectangular grid is placed over the simulation XY plane and the amphiphiles are assigned to grid cells according to the X, Y coordinates of their head beads. The upper monolayer contains those amphiphiles whose head Z coordinates are greater than their tail Z coordinates. The lower monolayer contains all other amphiphiles. This defines the number of amphiphiles in each monolayer. The average Z coordinate of the head beads in each grid cell for each monolayer is used to define the height of the monolayers at each point (X, Y). This procedure yields a two-dimensional height field, $h(X, Y)$, for each monolayer. The bilayer thickness is the difference between these heights averaged over all grid points, and the surface area of each monolayer is the sum of the areas of the triangles composing them. The grid cell width is typically twice the bead radius, so that there are at least several amphiphiles per cell. This smears out the protrusions of single amphiphiles from the monolayers, ensuring that the monolayer width and area are not overly sensitive to small-scale fluctuations.

The lateral density profiles of the hydrophobic and hydrophilic beads in the HC_6 bilayer, together with the water beads, are shown in Fig. 2. The profile in Fig. 2(a) is calculated with all chain beads included in the density, whereas that in Fig. 2(b) shows the distribution of the terminal chain bead only. It is clear from these profiles, and the snapshots in Fig. 1, that the amphiphiles are disordered within each monolayer, with their head groups confined to the solvent–
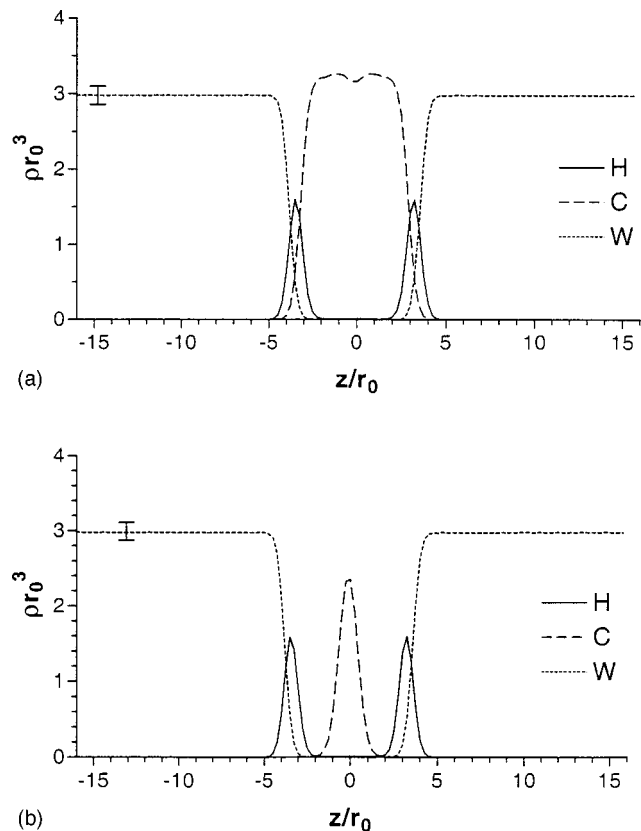

FIG. 2. (a) Bead number density profiles, ρr_0^3, for amphiphile head, H, and chain, C, beads in the bilayer of Fig. 1 and the bulk water, W. The simulation box is divided into 128 slices of thickness $r_0/4$ parallel to the bilayer surface, and 1000 samples of the number of beads of each type in the slices are used to construct the density profiles. Water is excluded from the bilayer interior by the strong hydrophobic repulsion of the chain beads, and the head beads are localized at the water–hydrophobic interface. All chain beads are included in the tail density profile, and it shows that the density in the hydrophobic region is uniform, except for a small dip at the bilayer midplane. The lower graph, (b), shows data from an independent simulation with the same parameters, but only the final chain bead contributes to the tail density distribution. The narrow peak indicates that the amphiphiles terminate near the bilayer midplane. All error bars are similar to the one shown, and indicate the statistical accuracy of the ensemble averages extracted from a single simulation.

hydrophobic interfaces and their terminal tail beads close to the bilayer midplane, and that the two monolayers are not very interdigitated in keeping with the L_α order of fluid-phase lipid bilayers. The profiles are calculated by averaging the bead densities over thin slices (of width $r_0/4$) parallel to the bilayer surface. The water is excluded from the hydrophobic region of the bilayer by the strong chain–water repulsion, whereas the head beads can sometimes penetrate to the center, although this is hardly visible in this figure. Two effects contribute to this penetration: amphiphiles can burrow their way through the bilayer emerging into the apposed monolayer, a process known as "flip–flop;" and the thermally excited shape fluctuations of the bilayer lead to density profiles that include contributions from nonplanar bilayer configurations. The chain bead density shows a small dip at the midplane of the bilayer, indicating that the monolayers are not significantly interdigitated. Bilayers composed of linear amphiphiles HC_n with $n = 4–10$ exhibit these general properties, although the shape fluctuations are larger for

shorter-chain amphiphiles. Amphiphiles containing four or more chain beads are not observed to leave the bilayer and exchange with the solvent on the time scale of the simulations, which is of the order of tens of nanoseconds.

Although a bilayer forms from HC_n surfactants for a wide range of (sufficiently large) tail–water repulsions, a_{CW}, two constraints should be satisfied before the simulated bilayer has properties that match the typical structure of a lipid bilayer. The average amphiphile end-to-end length should be approximately one-half of the bilayer thickness, so that the two monolayers do not interdigitate, and the amphiphiles should be oriented along the bilayer normal. We present results for a region of the simulation parameter space satisfying these constraints by adjusting the bond stretching and stiffness potential parameters. Under these constraints, the amphiphile length can be meaningfully compared to that of lipid molecules, and the bilayer thickness scales linearly with the amphiphile tail length. The end-to-end length, l_{ee}, of an HC_n amphiphile is measured from the center-to-center distance from the H bead to that of the last C bead. Two bond types are present in these amphiphiles: HC and CC, although, for simplicity, both types have the same bond strength parameters of $k_2 r_0^2 / k_B T = 128$, $l_0 / r_0 = 0.5$. These values yield average bond lengths of $\langle l_{HC} \rangle / r_0 = 0.62 \pm 0.01$ and $\langle l_{CC} \rangle / r_0 = 0.55 \pm 0.01$. The larger $\langle l_{HC} \rangle / r_0$ length reflects the repulsion of the head from the chain beads, and its greater freedom to fluctuate into the adjacent water than is possessed by chain beads deeper in the hydrophobic bulk. The standard deviation of the bond lengths is less than 2% for all tail lengths and bilayer tensions. The amphiphile end-to-end length for the tensionless HC_6 bilayer is $\langle \ell_{ee} \rangle / r_0 = 3.23 \pm 0.01$, which can be compared with the bilayer thickness $\langle \ell_{me} \rangle / r_0 = 6.61 \pm 0.01$, showing that the two monolayers are not interdigitated.

The end-to-end length grows linearly with the number of tail beads for all HC_n amphiphiles for a given chain stiffness $k_3 / k_B T$, as shown in Fig. 3(a), and is only slightly affected by the tension on the bilayer in the regime we study. It decreases slowly as the projected area per amphiphile, $A_{pr} / N r_0^2$, increases, with the decrease being larger for longer amphiphiles. For HC_8 amphiphiles, it decreases from $\langle \ell_{ee} \rangle / r_0 = 4.28 \pm 0.01$ for $A_{pr} / N r_0^2 = 0.60$ to $\langle l_{ee} \rangle / r_0 = 4.24 \pm 0.005$ for $A_{pr} / N r_0^2 = 0.64$. The surface tension increases from $\sigma r_0^2 / k_B T = -3.0$ to $\sigma r_0^2 / k_B T = 7.3$ over this span of areas, showing that HC_8 bilayers are stiff and strongly resist stretching. Note that the membrane buckles as soon as the negative tension exceeds a threshold value, as indicated in Fig. 11. Figure 3(b) shows that the bilayer thickness, l_{me}, divided by the amphiphile end-to-end length, l_{ee}, decreases as the area per amphiphile increases for HC_4 to HC_{10} amphiphiles. The product of membrane thickness and area is not constant, however, because the two monolayers increasingly interdigitate as the area increases. That it is monolayer interdigitation that occurs and not amphiphile shortening is shown by the small change in amphiphile lengths, of the order of 1%, over the span of areas considered. All of our results for tensionless bilayers are taken from the regime $\langle l_{me} \rangle / \langle l_{ee} \rangle \approx 2.0$, in which the monolayers are not significantly interdigitated. Bilayers composed of HC_6 or longer

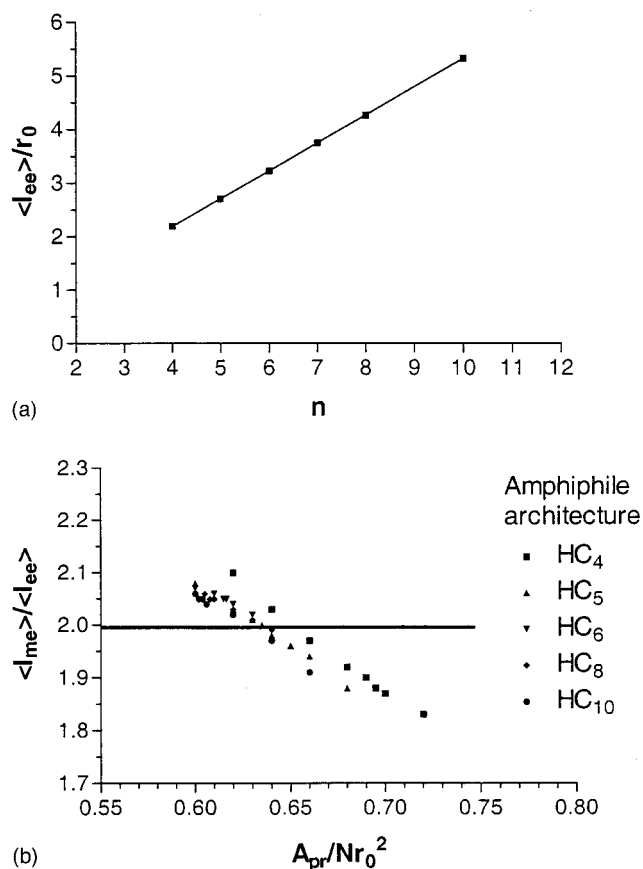FIG. 3. (a) End-to-end length $\langle \ell_{ee} \rangle / r_0$ of linear amphiphiles HC_n versus the number, n, of hydrophobic beads in the tail. The variation is linear with a slope of 0.52, showing that the polymers are kept straight by the chain stiffness potential given by Eq. (5). The end-to-end length changes by less than 1% for all amphiphile tail lengths and bilayer projected areas we present. (b) Variation of bilayer thickness, ℓ_{me}, divided by the amphiphile end-to-end length, as a function of the projected area per amphiphile. For $\langle \ell_{me} \rangle / \langle \ell_{ee} \rangle \approx 2$, the amphiphiles in the two monolayers are not interdigitated. The normalized thicknesses approximately collapse onto a single curve for amphiphiles with more than four tail beads.

amphiphiles are quite rigid, for the parameter set shown in Table I, and show only small shape fluctuations even close to zero surface tension. We provide an estimate of their bending rigidity in the next section.

At small values of $A_{pr} / N r_0^2$, the HC_4 membranes show substantial shape fluctuations that are increasingly suppressed for amphiphiles with longer tails. In addition, a tensionless state could not be found for HC_4 bilayers, given the parameter set of Table I, simply by varying the projected area because some amphiphiles inverted and buried their heads inside the hydrophobic region generating a positive surface tension. A well-ordered bilayer forms with a projected area of $A_{pr} / N r_0^2 = 0.70$, and surface tension $\sigma r_0^2 / k_B T = 0.013 \pm 0.016$, when the head–water conservative repulsion parameter is decreased from $a_{HW} r_0 / k_B T = 35$ to $a_{HW} r_0 / k_B T = 27$, keeping all other potential parameters unchanged. Increasing $A_{pr} / N r_0^2$ for all bilayers composed of HC_n amphiphiles reduces their shape fluctuations and thickness and, beyond a certain point, ruptures the membranes by the appearance of a pore. The amphiphiles around the pore rim reorient so as to shield their hydrophobic tails from the sur-

rounding solvent (data not shown). Although interesting as a possible model of pore formation, we do not investigate bilayer rupture further here. A simulation study of the rupture of amphiphile bilayers due to the presence of a cosurfactant has just been published.[36] We comment on the differences to our work in the Conclusions.

In the absence of chain stiffness, $k_3/k_B T = 0$, stable bilayers are formed in which the amphiphile tails represent (almost) freely jointed chains, but the hydrophobic region of the bilayer does not resemble two apposed monolayers (data not shown). Instead, the tails of amphiphiles in both monolayers are randomly intermixed. The hydrophilic head beads also show a tendency to penetrate into the hydrophobic interior, an effect that decreases if a chain stiffness is imposed. A chain stiffness of $k_3/k_B T = 20$, and a preferred angle of $\phi_0 = 0$ causes the amphiphiles to align approximately parallel to the bilayer normal, as seen in Fig. 1, and leads to a bilayer of two apposed monolayers. Note that because the hydrophobic chain beads (C) do not correspond to individual methyl groups, the order in the simulated amphiphile tails cannot be directly compared to the hydrocarbon chain order obtained, for example, from NMR experiments.

B. Lateral stress profile for bilayers of linear amphiphiles

Lipid bilayers around cells and vesicles are often close to a tension-free state. The distribution of stresses within the bilayer is not, however, uniform. Recent calculations[33] indicate that the presence of cosurfactants, and hydrocarbon chain stiffness due to unsaturated carbon–carbon bonds, modulate the membrane stress distribution, and that this is important, for example, for the potency of anaesthetics.[48] We have measured the stress distribution within the model bilayers as a function of amphiphile tail length and stiffness, and the number of tails attached to the hydrophilic head group. In this section we present the results for linear HC_n amphiphiles, and Sec. III C presents the stress profile for double-tail amphiphiles.

The calculation of the stress tensor for a system composed of point particles interacting via continuous potentials is described in Ref. 29, which extends the earlier work of Schofield and Henderson.[47] In this method, the contributions to the stress profile of the bead–bead interactions, bond stretching, and chain stiffness potentials are averaged over thin slices parallel to the bilayer surface. We define the stress profile, $\sigma(z)$, as the difference of the normal and lateral components of the stress tensor summed over all potentials. For further details of the calculation, the reader is referred to previous work.[29] The stress profile for the HC_6 bilayer described in Sec. III A is shown in Fig. 4, and exhibits a very similar structure to that seen in the MD simulations of Ref. 29. The aspects of this structure attributed to the bond and chain stiffness potentials in Ref. 29, namely the negative peaks assigned to the Hookean bond potential and the inner positive peaks due to the chain stiffness, appear here because the same potentials are used to build the amphiphiles out of soft beads. However, the absence of Lennard-Jones potentials in our simulations does not visibly modify the stress profile, indicating that the infinite barrier of Lennard-Jones
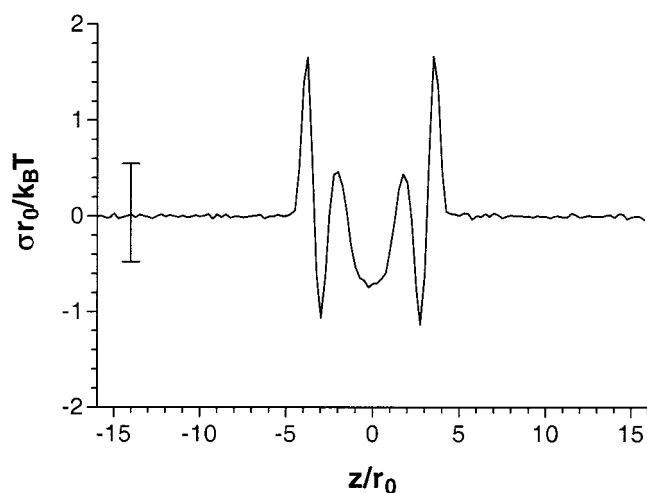

FIG. 4. Stress profile, $\sigma r_0/k_B T$, for the HC_6 bilayer shown in Fig. 1. The total stress is the sum of three contributions: (i) the repulsion potentials between head, tail, and water beads; (ii) the Hookean spring potentials connecting adjacent beads in the amphiphiles; and (iii) the chain stiffness potential between adjacent bonds in the amphiphiles. The outer positive peaks at the monolayer–water interfaces are due to the repulsion between the hydrophobic tail beads and the hydrophilic head and water beads. The adjacent negative troughs arise from the Hookean bond potential compressing the amphiphiles, while the inner positive peaks near the monolayer midplanes are due to the chain stiffness potential. Note that although the statistical errors in a single simulation are large, the shape of the stress profile is very similar in independent simulations and leads to a reproducible mean surface tension, as described in the text.

potentials is not essential for capturing the stress profile structure in mesoscopic simulations. The integral of $\sigma(z)$ across the bilayer yields the surface tension. We approximate this integral by a summation across the whole simulation box in the Z direction because the contribution from regions containing only solvent vanishes. We have used slices with widths $r_0/4$ and $r_0/8$, and the resulting surface tensions differ by less than the errors in the simulations. Even though the error bars for the stress tensor profile are quite large (see Fig. 4), the mean surface tension is highly reproducible in independent simulations. Additionally, the shape of the stress profile is very similar in independent simulations. The large error bars in the stress profile reflect the rapidly fluctuating forces acting on each bead, but the mean surface tension is integrated over the whole bilayer, and the individual bead fluctuations are smoothed out. The errors quoted for bilayer surface tensions are obtained from several independent simulations, each of which has a different initial set of bead coordinates and momenta, and uses a different sequence of random numbers. So, for example, eight repeated simulations of the bilayer shown in Fig. 1 produced surface tensions 0.048, −0.028, 0.029, 0.099, −0.016, 0.050, 0.016, −0.021. These yield a mean value $\sigma r_0^2/k_B T = 0.02 \pm 0.04$, and this is the value quoted in the caption of Fig. 1. The statistical errors of other measured quantities, such as the bilayer thickness, amphiphile end-to-end length and bead density profiles, are much smaller than those of the stress profile, and so we quote the errors obtained from a single simulation for these other quantities.

The surface tension of bilayers near their tensionless state can be very sensitive to changes in the area per am-
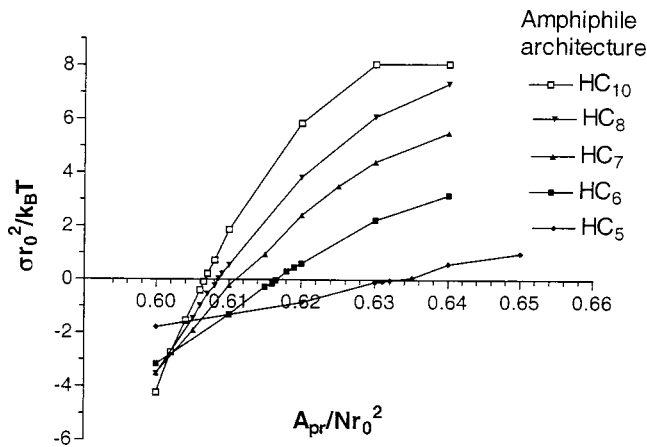
FIG. 5. Variation of the surface tension, $\sigma r_0^2/k_B T$ with the projected area per amphiphile, A_{pr}/Nr_0^2, for bilayers composed of HC_n amphiphiles for several tail lengths. The surface tension is obtained by first averaging the stress profile over slices parallel to the bilayer surface, and then integrating the averaged profile across the whole simulation box. The profile vanishes outside the bilayer region, as shown in Fig. 4. The lines connecting the points are only to guide the eye, but show that the surface tension varies linearly around its zero point and exhibits a sublinear dependence on area at large areas. The preferred area per amphiphile, at which the surface tension vanishes decreases as the amphiphile tail length increases.
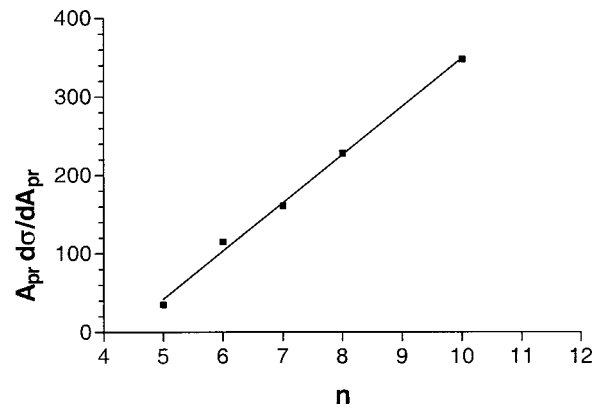

FIG. 6. Slope of the surface tension curves of Fig. 5, near their zero crossing point, with respect to the projected area per amphiphile for bilayers composed of HC_n amphiphiles. The data are obtained by a linear fit to the regions of the curves where the surface tension changes sign, and have been normalized by the preferred area. The bilayer area stretch modulus, K_n, measured from the rate of change of the surface tension with projected area, increases linearly with amphiphile tail length, n. A linear least-squares fit to the data yields $K_n r_0^2/k_B T = (61 \pm 2)n - (265 \pm 16)$.

phiphile. Adding or removing just three amphiphiles from the tensionless HC_6 bilayer of Fig. 1, which contains 3321 amphiphiles, changes its surface tension from $\sigma r_0^2/k_B T = 0.02 \pm 0.04$ to $\sigma r_0^2/k_B T = -0.15$ and $\sigma r_0^2/k_B T = 0.10$, respectively. The surface tensions for an HC_8 bilayer containing 3368, 3365, 3362 amphiphiles in a fixed simulation box of size $(32r_0)^3$ are $\sigma r_0^2/k_B T = -0.24$, 0.024, 0.21, respectively. This sensitivity reflects the large area stretch modulus for these bilayers, which increases rapidly with increasing amphiphile tail length. Although the equilibrium bilayer structure is insensitive to the exact value of the tail–water repulsion parameter in the range $a_{CW}r_0/k_B T = 65-85$, the thickness of the bilayer changing by less than 0.2% to 6.60 ± 0.01 and 6.62 ± 0.01 for the two extreme values, the peak heights in the lateral stress profile, and the surface tension, are sensitive to this parameter. Changing $a_{CW}r_0/k_B T$ for the bilayer of Fig. 1 to 65 and 85 changes the surface tension from approximately zero to $\sigma r_0^2/k_B T = -0.58$, 0.55, respectively, all other parameters being constant. This has the effect of moving the tensionless bilayer state to higher and lower projected areas, respectively.

The variation of the surface tension with projected area for bilayers formed of HC_5 to HC_{10} amphiphiles is shown in Fig. 5. The surface tension increases as A_{pr}/Nr_0^2 increases, the increase being steeper for amphiphiles with longer tails, and becomes sublinear at large values of the projected area. These results are very similar to those found in Ref. 29 using coarse-grained MD simulations (see their Figs. 7 and 8). The surface tension varies approximately linearly near zero tension, and amphiphiles with longer tails form stiffer bilayers for which a small change of area produces a large tension. We assume a dependence of the surface tension, Σ, on the bilayer projected area, A, and amphiphile tail length, n, of the form[29]

$$\Sigma(A, n) \approx K_n[A - A_0(n)]/A_0(n), \quad (6)$$

where $A_0(n)$ is the projected area at zero surface tension and K_n is the area stretch modulus of a bilayer formed of amphiphiles with tail length n. Figure 6 shows that the area stretch modulus increases linearly with the length of the hydrophobic tail. After scaling the surface tension by the preferred area, the compressibility is $K_n r_0^2/k_B T = (61 \pm 2)n - (265 \pm 16)$. Taking $k_B T$ as room temperature and assuming $r_0 \approx 1$ nm yields, for bilayers with $n = 6$, $K_6 \approx 418$ dyn/cm. By a similar calculation, the area stretch modulus of a bilayer composed of HC_5 amphiphiles is $K_5 \approx 166$ dyn/cm. These values are comparable to recent measurements of the area stretch modulus of 18-carbon diacyl phosphatidylcholine vesicles,[14] which yield $K \approx 243$ dyn/cm. If we compare the thickness of the simulated HT_5 membrane, $\langle \ell_{me} \rangle/r_0 = 5.4$, with the width of a typical 18-carbon diacyl lipid bilayer,[14] 4 nm, we see that the HT_5 amphiphiles are somewhat longer than 18-carbon lipids, and each DPD hydrophobic bead corresponds to three or four methyl groups.

We can extract an estimate for the bilayer bending rigidity, κ, using the relation $\kappa = K\ell_{me}^2/48$ from Ref. 30. Noting that the thickness of the tensionless HC_6 bilayer is $\langle \ell_{me} \rangle/r_0 = 6.61 \pm 0.01$, gives $\kappa \approx 90 k_B T$. This is larger than a typical value for one-component lipid bilayers,[14] which is of the order of $\kappa \approx 24 k_B T$ for dioleoylphosphatidylcholine (DOPC), but we note that cholesterol-containing lipid bilayers such as dimyristoylphosphatidylcholine (DMPC) with 30 mol.% cholesterol sulphate[10] have $\kappa \approx 91 k_B T$. However, repeating the calculation for the HC_5 bilayer, using Fig. 5 to find the projected area of the tensionless state and Fig. 3 to obtain the bilayer thickness, $\langle \ell_{me} \rangle/r_0 = 5.4$, together with the above relation for K_n, results in the smaller value $\kappa = 24 k_B T$. The close agreement with κ for DOPC is fortuitous, but suggests that the HT_5 amphiphiles form bilayers whose elastic properties are comparable to those of typical lipid bilayers. The stiffness of the simulated bilayers arises mainly from the tail bending stiffness potential, which is

needed to keep the amphiphiles in their separate monolayers, and its rapid increase with amphiphile tail length is consistent with the mean-field theory prediction that the bending energy of single-component amphiphilic films increases strongly with tail length.[26]

Reducing the chain stiffness for HC_6 amphiphiles to $k_3/k_BT = 10$, while keeping all other parameters constant, causes the bilayer shown in Fig. 1 to increase in thickness as some amphiphiles invert so that their heads are buried in the hydrophobic region (data not shown). This creates a large positive surface tension, $\sigma r_0^2/k_BT = 1.62$, across the bilayer. The surface tension remains positive as the projected area is varied, although it reaches a minimum, and the bilayer regains some of its ordered nature, for $A_{pr}/Nr_0^2 = 0.7$, at which point the mean bilayer thickness is $\langle \ell_{me} \rangle/r_0 = 5.71 \pm 0.03$. The bilayer may be restored to a tensionless state by reducing the head–water repulsion parameter, $a_{HW}r_0/k_BT$ to 30, and increasing the projected area to $A_{pr}/Nr_0^2 = 0.71$, but this reduces the chain order in the hydrophobic region, and leaves the bilayer thickness at $\langle \ell_{me} \rangle/r_0 = 5.72 \pm 0.02$. This result shows that the chain bending stiffness and amphiphile head–water repulsion parameters cannot be independently varied to produce a tensionless bilayer, but that they play effectively opposite roles in controlling the tendency of amphiphiles to invert and bury their heads in the hydrophobic region. Reducing the chain stiffness of amphiphiles in a tensionless bilayer requires a simultaneous reduction in their head–water repulsion, and an increase in the projected area, to restore the bilayer to a tensionless state. This behavior agrees qualitatively with experimental data[49] that increasing the lipid head group size stabilizes the L_α phase of lipid hydrocarbon tails with respect to the inverted hexagonal, H_{II}, phase, whereas reducing the amphiphile chain stiffness, thereby increasing the tail entropy, destabilizes the L_α phase.

In addition to the hydrophobic tail length, another key amphiphile property that determines the bilayer structure is the size of the hydrophilic head group. A planar bilayer is readily formed from amphiphiles of the form H_3C_6 in which three head and six chain beads are connected in a linear chain. The bead repulsion parameters and bond strengths are as shown in Table I, and the bending stiffness for HCC and CCC bead triples is $k_3/k_BT = 20$, while that of HHH and HHC bead triples is zero. This parameter set assigns a chain stiffness only to the bonds connecting pairs of hydrophobic beads, allowing the head beads to mimic a bulky head group rather than a linear one. The bead density profiles are very similar to that of Fig. 2 with the width of the head bead curve increasing for larger head group sizes, and the lateral stress distribution has the same structure as that shown in Fig. 4, except that the peak heights are modulated by the size of the head group (data not shown). Figure 7 shows the variation of the surface tension with the area per amphiphile for bilayers composed of HC_6, H_2C_6, and H_3C_6 amphiphiles. The area per amphiphile in the tensionless state increases strongly with the number of head beads, i.e., the area per amphiphile, while the bilayer area stretch modulus, which is related to the slope of the surface tension curve, decreases. These results are in agreement with mean-field predictions of bilayer bending elasticity.[26] Comparing these results with Fig. 5 shows
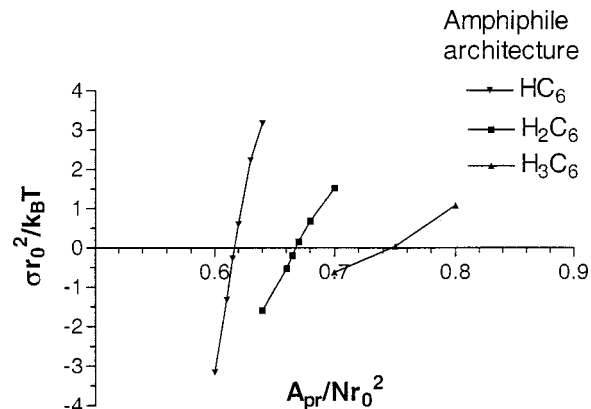

FIG. 7. Variation of the surface tension, $\sigma r_0^2/k_BT$, with the projected area per amphiphile, A_{pr}/Nr_0^2, for bilayers composed of H_mC_6 amphiphiles with $m = 1,2,3$. The tensionless bilayer state occurs at an area per amphiphile that increases with the number of head beads, while the slope of the tension near its zero-crossing point decreases with head group size. This indicates that larger head groups push the amphiphiles farther apart and reduce the bilayer stiffness.

that decreasing the hydrophobic tail length or increasing the number of head beads both force the amphiphiles apart, and lead to a larger area per amphiphile in the tensionless bilayer state.

C. Results for bilayers composed of double-tail amphiphiles

Although vesicles made of single-tail surfactants are of great current interest,[3,4] naturally occurring lipid bilayers typically consist of double-tailed lipids. A more realistic amphiphile architecture for lipid membranes is thus $H_m(C_n)_2$ in which two tails, each containing n hydrophobic beads, are attached to a head composed of m hydrophilic beads. We have used architectures with two to four head beads, and tails containing four or six beads. Unless otherwise stated, all bead–bead, bond, and chain stiffness potential parameters are the same as for the single-tail amphiphiles.

Adding an extra tail to a single hydrophilic head bead destroys the lamella order in the simulated bilayers. The second tail almost doubles the amphiphile volume while leaving the head area unchanged, and the small head is unable to shield the hydrophobic tails from the solvent. Increasing the effective head group size by adding extra head beads restores the ordered bilayer. Therefore we consider first the architecture $H_3(C_6)_2$ in which the head beads are attached in a linear sequence, and the tails are attached to two adjacent head beads. This architecture should be distinguished from that of previous simulations[43] of diblock copolymers in which all beads are connected in a single linear sequence, and also from a previous DPD lipid bilayer simulation[36] because of the quite distinct interaction parameters. The amphiphiles in Ref. 36 have, in our notation, an $H_2H'(C_5)_2$ architecture, in which two head bead types, H and H' are attached to two tails of C beads that have no chain stiffness; and the H, H' beads are as strongly repelled from the C beads as are the solvent beads. Our parameter set in Table I only assumes a strong repulsion between solvent and tail beads, in order to represent the hydrophobic effect, and the head–tail and
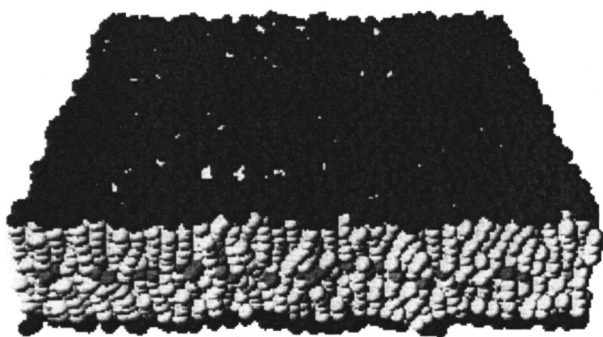
FIG. 8. Snapshot of a bilayer containing 1685 $H_3(C_6)_2$ amphiphiles. The simulation box has size $(32r_0)^3$, and the bead density is $\rho r_0^3 = 3$, giving almost 100 000 beads of all types. The projected area per amphiphile is $A_{pr}/Nr_0^2 = 1.215$, leading to a surface tension of $\sigma = -0.05 \pm 0.05$. The amphiphile head beads are dark gray, and the tail beads are light gray, except for the terminal one, which is darker. Water beads are invisible for clarity. The average membrane thickness, measured from the center of the first head bead of the amphiphiles in one monolayer to those of the other, is $\langle \ell_{me} \rangle / r_0 = 7.05 \pm 0.25$. The larger standard deviation of the bilayer thickness here compared to that in Fig. 1 arises from the greater freedom of the first head bead in $H_3(C_6)_2$ amphiphiles, which is unattached to the tails, to move around. Thermally excited shape fluctuations are small here because of the chain stiffness of the amphiphiles.

FIG. 9. Bead number density profiles, ρr_0^3, for the first amphiphile head bead, H, and last tail bead, C, in the bilayer of Fig. 8 and the bulk water, W. This can be compared with the lower graph in Fig. 2. The head bead is confined to the water–hydrophobic interfacial region while the last tail bead is restricted to the bilayer midplane, showing that the tails are relatively straight. The areas under the H and C curves yield the number of beads of those types in the simulation box. Because only the first and last beads are used to construct the profiles, the areas give the number of amphiphiles in the bilayer. The difference between the peak heights in Fig. 2 and this figure reflect the different numbers of amphiphiles in the two bilayers: 3321 single-tail amphiphiles and 1685 double-tail amphiphiles, respectively.

head–solvent repulsions are relatively weak. The properties of the resulting bilayers are sensitive to the head–tail and head–solvent repulsion parameters, and this indicates that a detailed study of their effects is required in order to map the varying degrees of hydrophilicity of lipid head groups onto the simulation's parameter space.

A typical configuration of a membrane containing 1685 $H_3(C_6)_2$ amphiphiles is shown in Fig. 8. The membrane is close to a tension-free state with a projected area of $A_{pr}/Nr_0^2 = 1.215$ and a surface tension of $\sigma r_0^2 / k_B T = 0.03 \pm 0.08$. As for the linear amphiphiles of Sec. III B, this value is the average of several independent simulations. The tail bead farthest from the first head bead is colored darker solely for display purposes. The second tail almost doubles the amphiphile volume and tail area for fixed tail length, and increases the $\langle A \rangle / Nr_0^2$ of the tensionless state. The mean bond lengths in the $H_3(C_6)_2$ amphiphiles are almost the same as for the HC_n amphiphiles: $\langle l_{HC} \rangle / r_0 = 0.63 \pm 0.01$ and $\langle l_{CC} \rangle / r_0 = 0.54 \pm 0.01$, and these values are independent of the tension on the bilayer. The length of the bonds connecting the head beads is $\langle l_{HH} \rangle / r_0 = 0.55 \pm 0.01$, and the distance from the first head bead to the last tail bead is $\langle \ell_{ee} \rangle / r_0 = 3.67 \pm 0.01$. This is only slightly larger than the end-to-end length of the HC_6 amphiphiles, which is $\langle \ell_{ee} \rangle / r_0 = 3.23 \pm 0.01$, and shows that the multiple head beads in the double-chain amphiphiles are closely grouped and may provide a reasonable model for the bulky head groups of some lipids. The density profiles of the head and tail beads for this bilayer are shown in Fig. 9. The terminal tail beads are located close to the bilayer midplane, and the width of the head bead distribution is comparable to that in Fig. 2, but its height is smaller. The area under the peaks yields the number of head beads in the simulation. This is the same as the number of amphiphiles because the HC_6 amphiphiles have one head bead per amphiphile, and only the first head bead is
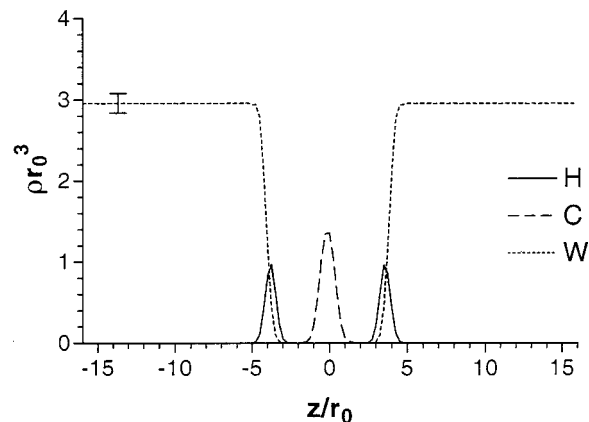
used to calculate the density for the $H_3(C_6)_2$ amphiphiles. Hence, the areas under the head bead distributions, multiplied by the monolayer surface area, gives the number of amphiphiles in each bilayer and this accounts for the decrease in peak height for the double-tail amphiphiles. The lateral stress profile for the $H_3(C_6)_2$ bilayer is shown in Fig. 10, and is qualitatively similar to that of Fig. 4. The positive peaks near the center of the hydrophobic region have been reduced in magnitude, as have the negative peaks. The surface tension is less sensitive to the number of head beads in $H_m(C_6)_2$ amphiphiles than to their tail length, as shown in Fig. 11. At a projected area of $A_{pr}/Nr_0^2 = 1.21$, the surface tension of bilayers composed of $H_3(C_6)_2$ and $H_4(C_6)_2$ am-
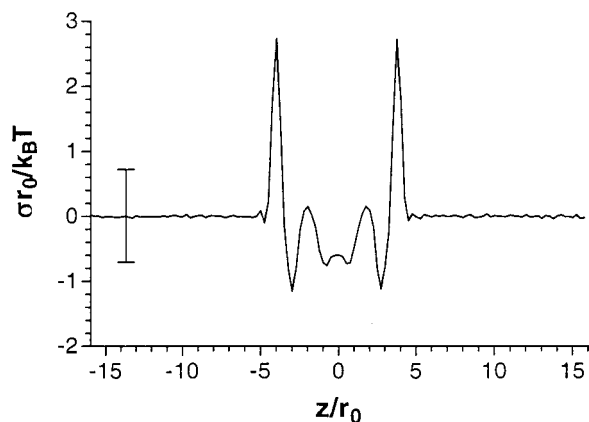

FIG. 10. Stress profile, $\sigma r_0 / k_B T$, for the $H_3(C_6)_2$ bilayer of Fig. 8. The total stress is the sum of three contributions: (i) the repulsion potentials between head, tail, and water beads; (ii) the Hookean spring potentials connecting adjacent beads in the amphiphiles; and (iii) the chain stiffness potential between adjacent bonds in the amphiphiles. Note that although the typical statistical error bars from a single simulation are quite large, the mean surface tension is reproducible between independent simulations.
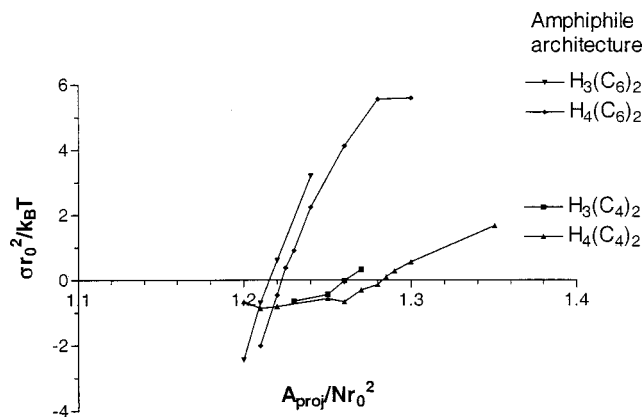
FIG. 11. Surface tension, $\sigma r_0^2/k_B T$, for bilayers composed of $H_m(C_n)_2$ amphiphiles as a function of the projected area per amphiphile, A_{pr}/Nr_0^2, for head group sizes $m=3,4$ and tail lengths $n=4,6$. The tensionless bilayer state occurs at an area per amphiphile that increases with the number of head beads, and decreases with increasing tail length. This is similar to the results found for the single-tail amphiphiles, but the dependence of the preferred area on the number of head beads is weaker, and the slope of the surface tension curves is roughly independent of head group size for amphiphiles with two tails.

phiphiles is $\sigma r_0^2/k_B T = -0.8$ and $\sigma r_0^2/k_B T = -2.0$, respectively. For these two cases the bilayers are still flat (data not shown), which indicates that the negative values of surface tension have not yet exceeded their threshold values for buckling. The bulkier head groups push the amphiphiles farther apart, shifting the preferred area to slightly higher values. This shift is less significant than that shown in Fig. 7 for bilayers composed of single-tail amphiphiles. Comparing Fig. 7 and Fig. 11 also shows that the slope of the surface tension curve near its zero crossing does not greatly depend on the head group size for double-tail amphiphiles, whereas it decreases significantly for the single-tail amphiphiles.

Amphiphiles with the architecture $H_3(C_4)_2$ form well-ordered, tensionless bilayers whereas linear amphiphiles with the same number of hydrophobic beads, HC_4, and the same interaction parameter set, do not. The thickness of the tensionless $H_3(C_4)_2$ bilayer is $\langle \ell_{me}\rangle/r_0 = 4.73 \pm 0.01$ compared to an amphiphile end-to-end length $\langle \ell_{ee}\rangle/r_0 = 2.67 \pm 0.01$. For comparison, the thickness of the $H_3(C_6)_2$ bilayer shown in Fig. 8 is $\langle \ell_{me}\rangle/r_0 = 7.36 \pm 0.03$ compared to an amphiphile end-to-end length $\langle \ell_{ee}\rangle/r_0 = 3.67 \pm 0.01$. The preferred area for the $H_3(C_4)_2$ bilayer is $A_{pr}/Nr_0^2 = 1.26$, at which the surface tension is $\sigma r_0^2/k_B T = -0.01 \pm 0.05$. This is a larger preferred area than that of the bilayer formed from $H_3(C_6)_2$ amphiphiles, showing that the longer tails lead to more closely packed bilayers as found for the single-tail amphiphiles. Reducing the chain stiffness of the double-tail amphiphiles leads to bilayers with larger shape fluctuations, but does not destroy the lamellar order as it does for membranes composed of single-tail amphiphiles. An observation of the bilayer state shows that very few amphiphiles invert and bury their heads in the hydrophobic region. The difficulty of pulling the bulkier head group into the hydrophobic region appears to stabilize the lamella state.

IV. DISCUSSION AND CONCLUSIONS

We have used Dissipative Particle Dynamics simulations to investigate the equilibrium structure of amphiphilic bilayers, and to measure their lateral stress profile and its dependence on the amphiphile architecture. Although we mainly compare model bilayer properties to typical lipid bilayers,[2] the results are applicable to any mesoscopic amphiphilic system such as the recently created polymersomes[5] or nonbiological vesicles.[18] The ability to extract the mesoscopic properties of aggregates composed of amphiphiles with complex architectures, such as multiple hydrophobic tails or polymers with hydrophilic side chains, and to allow the amphiphile interactions to vary with their architecture, makes simulations a valuable complementary technique to theoretical predictions for homogeneous bilayers.[21–27] A typical bilayer in our work contains 3200 amphiphiles and although the effective potentials used in DPD lack a direct link to the molecular interactions of the amphiphilic molecules being represented, this loss should not be significant for the determination of material properties that represent averages over a large number of molecules.

Linear amphiphiles with an HC_n architecture immersed in bulk water readily self-assemble into a bilayer if their hydrophobic tails are sufficiently strongly repelled by the water beads. Amphiphiles with four or less tail beads do not form well-ordered bilayers, whereas ones with five or more beads per tail form progressively stiffer bilayers. The hydrophobic region of the bilayers is relatively structureless and does not resemble the two apposed monolayers of lipid bilayers unless a chain stiffness potential is imposed on the hydrophobic tails to mimic the stiffness of hydrocarbon chains. In addition, the two monolayers tend to interdigitate unless the amphiphile end-to-end length is constrained by a strong Hookean bond potential between adjacent tail beads in addition to the (repulsive) bead–bead interaction. Because a hydrophobic bead in our simulations represents several methyl groups in a hydrocarbon chain, the model amphiphile tails should not be expected to possess the same degree of order as lipid hydrocarbon tails. But we expect that the mesoscopic organization of the hydrophobic region of a bilayer, viz., two apposed monolayers of hydrocarbon chains with anisotropic fluid order and only slight overlap at the bilayer midplane, should be retained in the simulations. These restrictions on the chain potentials lead to bilayers whose equilibrium static properties (thickness, area per amphiphile) correspond qualitatively with those found in experimental lipid bilayer systems. Amphiphiles with five or more hydrophobic beads do not leave the bilayer on the time scale of the simulations that approaches a microsecond of real time. Increasing the amphiphile tail length, keeping all the interaction parameters fixed, leads to stiffer bilayers, for which a small change in the area per lipid results in a large change in the surface tension. Whereas a uniform hydrophobic region density is an assumption of some mean-field theories,[21] it arises naturally in the simulations. At the bilayer midplane a small dip in the density reflects the greater conformational freedom of the terminal tail beads near the bilayer midplane.

More complicated amphiphile architectures lead to bilayers whose structure and material properties are modulated

by the relative head-to-tail size. Increasing the tail volume by reducing the chain stiffness destabilizes the bilayer, as some amphiphiles bury their heads inside the hydrophobic region. This effect is opposed by increasing the effective head group volume by, for example, adding more hydrophilic beads to the head group or reducing the repulsion of the head beads from the solvent. These results are qualitatively similar to experimental data on lipid systems,[49] and previous microscopic models of lipid phase behavior.[24] Amphiphiles possessing two hydrophobic tails require three or more head beads to shield the tails from the surrounding solvent, and form a well-ordered bilayer. They are also able to form well-ordered bilayers with shorter tails than is possible for the single-tailed amphiphiles. Additionally, reducing the chain stiffness for double-tail amphiphiles, keeping all other parameters fixed, increases the shape fluctuations of the bilayer but does not destroy the lamella state as it does for the single-tail amphiphilic bilayers. These results show that although many combinations of simulation parameters may yield bilayers, not all such bilayer structures correspond quantitatively or qualitatively to, say, experimental lipid bilayers, and not all parameters can be independently varied. Reducing the amphiphile chain stiffness, for example, requires a reduction of the head–solvent repulsion parameter or an increase in the head group size, to restore the tensionless bilayer state. It may be possible to work in regions of the simulation parameter space so as to mimic, for example, amphiphiles possessing different physical properties, such as head group size, hydrophilicity, and tail stiffness. Several such amphiphilic species could then be formed into a bilayer or vesicle, and the properties of composite membranes explored. A comparison of the resulting aggregates with experimental data can be used to identify the parameter combinations most appropriate for representing selected amphiphiles.

The lateral stress profile across the bilayers exhibits structure that is qualitatively similar to that previously seen in coarse-grained Molecular Dynamics simulations,[29] and is sensitive to the amphiphile architecture. Several peaks are observed for single-tail amphiphiles, whose heights reflect the relative contributions of the bead–bead, bond strength, and chain stiffness potentials. Increasing the number of head beads or decreasing the hydrophobic tail length of linear amphiphiles shifts the tensionless bilayer state to larger membrane areas. Amphiphiles with two tails have quite similar stress profiles. The excellent qualitative similarity between the stress profiles produced in our DPD simulations and prior MD simulations, and the faster execution of DPD, suggests that studies of the stress distribution in bilayers may be more efficiently performed using DPD than coarse-grained MD.

In the absence of an external tension or osmotic stress, the lipids in a vesicle adopt their preferred area thereby minimizing their free energy. The preferred area per amphiphile for the model bilayer is found by measuring the surface tension as a function of the projected area until the state of zero surface tension is obtained. At small enough values of the area per amphiphile, such that the surface tension is sufficiently negative, the bilayer is buckled. As the projected area per amphiphile increases, the surface tension passes through zero to positive values for stretched bilayers. Assuming the

surface tension to vary linearly with projected area for tensions close to zero allows us to extract an estimate of the bilayer area compressibility modulus. We obtain the value $K = 418$ dyn/cm for amphiphiles with six tail beads. This may be compared to the experimental value[14] for lipid bilayers made of lipids with between 13 and 18 carbons of approximately 243 dyn/cm. When converted into an estimate of the bilayer bending rigidity using the relation[30] $\kappa = K \ell_{me}^2 / 48$, the simulated bilayer composed of amphiphiles with six hydrophobic tail beads has a bending rigidity of $90 k_B T$. This is approximately a factor of 4 larger than that for lipid bilayers containing only DOPC[14] for which $\kappa = 24 k_B T$. Simulated bilayers containing amphiphiles with 5 hydrophobic tail beads have a smaller bending rigidity, which we estimate to be $\kappa = 24 k_B T$ using the above relation. Given the coarse graining of a number of methyl groups to each DPD bead (see Sec. III B), this suggests that one DPD hydrophobic bead corresponds to three or four methyl groups.

Increasing the amphiphile head group size at a fixed chain length leads to an increased repulsion between amphiphiles, and the tensionless bilayer state occurs at a larger preferred area per amphiphile. These results are in qualitative agreement with the concept of ''opposing forces'' in lipid bilayers,[50] which states that the equilibrium bilayer structure is determined by the balance of the opposing tendencies of lipid hydrocarbon tails to aggregate in water and the steric repulsion of the phosphatidyl-glycerol head groups. This gives us confidence that the mesoscopic DPD method captures at least some of the physical properties of amphiphilic molecules necessary to allow it to be extended to simulations of more complex membrane phenomena.

A recent application of DPD investigates pore formation in a lipid bilayer induced by the presence of a nonionic cosurfactant.[36] The lipid architecture used is similar to our $H_3(C_4)_2$ amphiphiles. The lateral stress profile has some similarity to the current work and previous results,[29] but shows no central peaks. The authors suggest that the difference between their stress profile and that found in MD simulations[29] may be due to the lack of hard-core Lennard-Jones potentials in the DPD simulations. We present data showing that this is not the case: We find a similar stress profile in our DPD simulations as Ref. 29. Instead, we suggest that the absence of the central peaks in Ref. 36 is due to the absence of the chain stiffness potential. Our results show that ignoring the chain stiffness potential leads to entangled amphiphile conformations and interdigitation of the two monolayers. That this may be the case in Ref. 36 can be seen by comparing the spatial distribution of the terminal tail bead of the amphiphiles with our results. Figure 9 shows the density profiles of the head and terminal tail beads for the bilayer of Fig. 8. The terminal tail bead has a sharply peaked distribution close to the bilayer midplane, as expected for approximately straight amphiphiles. This is in contrast to the results of Ref. 36 (seen in their Fig. 4) in which the terminal tail bead distribution spans the entire hydrophobic region of the bilayer, and penetrates the hydrophilic head region. The soft beads in DPD simulations require additional constraints, imposed by the chain stiffness potential, to create well-

ordered bilayers, whereas the infinite core and attractive piece of the Lennard-Jones potential are sufficient to create well-ordered bilayers in coarse-grained MD simulations.

A major goal of computer simulations is to predict the material properties of mesoscopic, or possibly macroscopic, aggregates given only the elementary molecular constituents composing them. Although, perhaps, less useful for simulating interactions between hard colloidal particles in solution, DPD shows great promise when applied to soft complex fluids. We have shown that model amphiphiles consisting of a hydrophilic headgroup attached to one or two hydrophobic tails form planar bilayers whose density profile and lateral stress distribution, and the dependence of these properties on the amphiphile architecture, agree at least qualitatively with experiments, previous coarse-grained MD simulations, and microscopic theories of lipid phases. The task of capturing just those microscopic properties of amphiphiles that give rise to the material properties and dynamical behavior of lipid bilayers or polymersomes, is a challenge whose solution will have direct applications to chemistry, materials science, and medicine. Cell membrane fusion is one example for which an improved understanding would greatly assist drug development. Some simulation studies of fusion have recently appeared in the literature,[51,52] but these studies either ignore the solvent molecules,[51] or use Monte Carlo simulations,[52] and thus generate trajectories that are not demonstrated to correspond to those of a particular set of Newtonian and hydrodynamic equations of motion. By contrast, the DPD method described here incorporates both the solvent molecules and their hydrodynamics. Using the DPD approach, we have already observed some fusion events and are confident that we will be able to simulate a realistic fusion dynamics.

[1] B. Alberts, D. Bray, J. Lewis, M. Raff, K. Roberts, and J. D. Watson, *Molecular Biology of the Cell*, 2nd ed. (Garland, New York, 1989).
[2] *Structure and Dynamics of Membranes*, Handbook of Biological Physics Vol. 1, edited by R. Lipowsky and E. Sackmann (Elsevier, Amsterdam, 1995).
[3] P. Walde, M. Wessicken, U. Raedler, N. Berclaz, K. Conde-Frieboes, and P. L. Luisi, J. Phys. Chem. **101**, 7390 (1997).
[4] B. zu Putlitz, K. Landfester, S. Foerster, and M. Antonietti, Langmuir **16**, 3003 (2000).
[5] B. M. Discher, D. A. Hammer, F. S. Bates, and D. E. Discher, Curr. Opin. Colloid Interface Sci. **5**, 125 (2000).
[6] R. Lipowsky, in *From Membranes to Membrane Machines*, in Statistical Mechanics of Biocomplexity, edited by D. Reguera, J. M. G. Vilar, and J. M. Rubi (Springer-Verlag, Berlin, 1999).
[7] *Vesicles*, edited by M. Rosoff (Marcel Dekker, New York, 1996).
[8] D. D. Lasic, in *Giant Vesicles*, Perspectives in Supramolecular Chemistry, edited by P. L. Luisi and P. Walde (Wiley, Chichester, 2000), Vol. 6.
[9] H-G. Doebereiner, O. Selchow, and R. Lipowsky, Eur. Biophys. J. **28**, 174 (1999).
[10] P. Meleard, C. Gerbeaud, T. Pott, L. Fernandez-Puente, I. Bivas, M. D. Mitov, J. Dufourcq, and P. Bothorel, Biophys. J. **72**, 2616 (1997).
[11] D. Needham and R. S. Nunn, Biophys. J. **58**, 997 (1990).
[12] A. Sonnleitner, G. J. Schuetz, and Th. Schmidt, Biophys. J. **77**, 2638 (1999).
[13] R. Dimova, C. Dietrich, A. Hadjiisky, K. Danov, and B. Pouligny, Eur. Phys. J. B **12**, 589 (1999).
[14] W. Rawicz, K. C. Olbrich, T. McIntosh, D. Needham, and E. Evans, Biophys. J. **79**, 328 (2000).
[15] K. Olbrich, W. Rawicz, D. Needham, and E. Evans, Biophys. J. **79**, 321 (2000).
[16] P. Broca, L. Cantu, M. Corti, and E. Del Favero, Prog. Colloid Polym. Sci. **115**, 181 (2000).
[17] C. Leidy, W. F. Wolkers, K. Jorgensen, O. G. Mouritsen, and J. H. Crowe, Biophys. J. **80**, 1819 (2001).
[18] C. A. McKelvey, E. W. Kaler, J. A. Zasadzinski, B. Coldren, and H.-T. Jung, Langmuir **16**, 8285 (2000).
[19] H-P. Hentze, E. Kraemer, B. Berton, S. Foerster, and M. Antonietti, Macromolecules **32**, 5803 (1999).
[20] R. G. Larson, J. Chem. Phys. **91**, 2479 (1989).
[21] D. Harries and A. Ben-Shaul, J. Chem. Phys. **106**, 1609 (1997).
[22] F. A. M. Leermakers and J. M. H. M. Scheutjens, J. Chem. Phys. **89**, 3264 (1988).
[23] D. R. Fattal and A. Ben-Shaul, Physica A **220**, 192 (1995).
[24] X-J. Li and M. Schick, Biophys. J. **78**, 34 (2000).
[25] M. Mueller and M. Schick, Phys. Rev. E **57**, 6973 (1998).
[26] I. Szleifer, D. Kramer, A. Ben-Shaul, D. Roux, and W. M. Gelbart, Phys. Rev. Lett. **60**, 1966 (1988).
[27] L. A. Meijer, F. A. M. Leermakers, and A. Nelson, Langmuir **10**, 1199 (1994).
[28] S. J. Marrink, E. Lindahl, O. Edholm, and A. E. Mark, J. Am. Chem. Soc. **123**, 8638 (2001).
[29] R. Goetz and R. Lipowsky, J. Chem. Phys. **108**, 7397 (1998).
[30] R. Goetz, G. Gompper, and R. Lipowsky, Phys. Rev. Lett. **82**, 221 (1999).
[31] E. Lindahl and O. Edholm, Biophys. J. **79**, 426 (2000).
[32] M. Laradji and O. G. Mouritsen, J. Chem. Phys. **112**, 8621 (2000).
[33] R. S. Cantor, Biophys. J. **76**, 2625 (1999).
[34] J. C. Shelley, M. Y. Shelley, R. C. Reeder, S. Bandyopadhyay, and M. L. Klein, J. Phys. Chem. B **105**, 4464 (2001).
[35] M. Venturoli and B. Smit, Phys. Chem. Commun. **10**, 1 (1999).
[36] R. D. Groot and K. L. Rabone, Biophys. J. **81**, 725 (2001).
[37] P. J. Hoogerbrugge and J. M. V. A. Koelman, Europhys. Lett. **19**, 155 (1992).
[38] P. Espagnol and P. Warren, Europhys. Lett. **30**, 191 (1995).
[39] C. A. Marsh, G. Backx, and M. H. Ernst, Phys. Rev. E **56**, 1676 (1997).
[40] P. Espagnol, Europhys. Lett. **40**, 631 (1997).
[41] I. Pagonabarraga, M. H. J. Hagen, and D. Frenkel, Europhys. Lett. **42**, 377 (1998).
[42] R. D. Groot and P. B. Warren, J. Chem. Phys. **107**, 4423 (1997).
[43] R. D. Groot and T. J. Madden, J. Chem. Phys. **108**, 8713 (1998).
[44] J. L. Jones, M. Lal, J. Noel Ruddock, and N. A. Spenley, Faraday Discuss. **112**, 129 (1999).
[45] J. C. Shelley and M. Y. Shelley, Curr. Opin. Colloid Interface Sci. **5**, 101 (2000).
[46] P. B. Warren, Curr. Opin. Colloid Interface Sci. **3**, 620 (1998).
[47] P. Schofield and J. R. Henderson, Proc. R. Soc. London, Ser. A **379**, 231 (1982).
[48] R. S. Cantor, Biophys. J. **80**, 2284 (2001).
[49] S. M. Gruner, J. Phys. Chem. **93**, 7562 (1989).
[50] C. Tanford, *The Hydrophobic Effect* (Wiley, New York, 1980).
[51] H. Noguchi and M. Takasu, J. Chem. Phys. **115**, 9547 (2001).
[52] M. Mueller, K. Katsov, and M. Schick, J. Chem. Phys. **116**, 2342 (2002).